Acta Materialia 265 (2024) 119623

Contents lists available at ScienceDirect

Acta Materialia

journal homepage: www.elsevier.com/locate/actamat

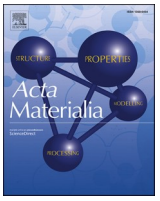

Full length article

Grain-level mechanism of plastic deformation in harmonic structure materials revealed by high resolution X-ray diffraction

Elis Sjögren-Levin [a,*], Wolfgang Pantleon [b], Aylin Ahadi [a], Zoltan Hegedüs [c], Ulrich Lienert [c], Nobuhiro Tsuji [d], Kei Ameyama [e], Dmytro Orlov [a]

[a] Department of Mechanical Engineering Sciences, Division of Mechanics, Materials and Components, LTH, Lund University, Box 118, Lund 22100, Sweden
[b] Department of Civil and Mechanical Engineering, Section of Materials and Surface Engineering, Technical University of Denmark, Kongens 2800, Lyngby, Denmark
[c] Deutsches Elektronen-Synchrotron (DESY), Hamburg 22607, Germany
[d] Department of Materials Science and Engineering, Kyoto University, Yoshida-honmachi, Sakyo-ku 606-8501, Kyoto, Japan
[e] Department of Mechanical Engineering, Faculty of Science and Engineering, Ritsumeikan University, 1-1-1 Nojihigashi, Kusatsu 525-8577, Shiga, Japan

ARTICLE INFO

Keywords:
Heterogeneous structure
Harmonic structure material
Synchrotron diffraction
Reciprocal space mapping
Plastic flow properties

ABSTRACT

Materials with heterogeneous microstructures have been reported to have an attractive combination of strength and ductility. This is attributed to synergistic strengthening effects from the difference in strength of fine- and coarse-grained regions. Understanding the interaction of the regions is crucial for further optimization of the microstructures. In this work, we fabricated nickel of harmonic structure (HS) and a reference with homogenous coarse grains. The HS constitutes of an interconnected fine-grained network that surrounds regions of coarse grains. The interplay of the regions was studied by monitoring Bragg reflections from individual grains *in situ* during tensile deformation until approximately 2 % strain through synchrotron X-ray diffraction. The technique allows grain-level assessment of the degree of plastic deformation. Two grains were followed in the reference and two small grains (fine-grained region) and two large grains (coarse-grained region) in the HS. Three deformation regimes were identified: elastic deformation, onset of plastic deformation and significant plastic deformation. Our results reveal that the large grains in the harmonic structure onset plastic deformation during the macroscopic elastic stage. With increasing applied stress, the small grains yield plastically also and once a large fraction of the fine-grained network deforms plastically the large grains undergo significant plastic deformation. Notably, the onset of significant plastic deformation of large grains in the HS occurs at approximately 100 MPa higher applied stress than in the grains in the reference. This shows that fine grains constrain the large grains from deforming plastically in the HS.

1. Introduction

Materials that are simultaneously strong and ductile are desirable in industrial applications. Unfortunately, metals strengthened through cold-working and grain refinement show in general a reduced ductility [1]. This is due to grains of small sizes such as nanocrystalline and ultrafine grains (UFG) having limited work-hardening capability leading to strain localization already at small strains [2,3]. To obtain materials that are simultaneously strong and ductile, heterogeneous microstructures with multimodal grain size distributions were developed [4] with the intention to combine the strength from small grains with the work-hardening ability of coarse grains. However, volume fraction and spatial distribution of small and coarse grains are difficult to control in heterogeneous structures produced by conventional thermomechanical processes [5,6]. Other architectured structures such as layered structures produced through stacking of thin foils or electrodeposition have better spatial control but are intrinsically anisotropic [7,8]. Harmonic structure (HS) materials are among the most promising heterogeneous microstructures produced through a route of powder metallurgy [9]. They possess an interconnected, fine-grained network (with ultrafine or nanocrystalline grains) that encapsulates regions of coarse grains. HS materials have homogeneous properties on the macroscopic scale as their heterogeneous grain structure is ordered but non-directional. Such a microstructure design has been applied on a number of pure metals and alloys, as summarized in [6,9–11]. In general, the application of HS has shown to be successful in terms of increasing strength without

* Corresponding author.
E-mail address: elis.levin@lth.lu.se (E. Sjögren-Levin).

https://doi.org/10.1016/j.actamat.2023.119623
Received 9 August 2023; Received in revised form 20 November 2023; Accepted 18 December 2023
Available online 21 December 2023

significant loss in ductility [6].

According to the Considère criterion, necking may occur when work-hardening rate equals the stress ($d\sigma/d\epsilon = \sigma$) for strain-rate insensitive materials [12,13]. As a reduction of grain size tends to increase the flow stress, the criterion is met at lower strains [3]. Heterogeneous structures are believed to delay the fulfilment of the criterion by increasing the work-hardening rate through a combination of synergetic effects [4,11]. The differences in plastic flow between coarse- and fine-grained regions at their common interface is expected to cause strain gradients. These strain gradients are accommodated by geometrically necessary dislocation densities [14] that increase the overall dislocation density and the work hardening rate.

Park et al. observed in HS indeed larger plastic strains in the coarse-grained regions than in fine grained regions and particularly steep strain gradients at their interfaces at 10 % macroscopic strain [15]. This result is consistent with analytical modelling [16] and finite-element simulations [17].

Coarse grains surrounded by fine grains in HS are expected to have a higher work-hardening rate than coarse grains surrounded by other coarse grains. In a recent study, we monitored the evolution of the average stresses along tensile direction separately for coarse-grained and fine-grained fractions in HS nickel by *in situ* X-ray diffraction up to 4.5 % strain [18]. The stress-strain curve of the coarse-grained fraction was compared with the curve of homogenous coarse-grained nickel. Yielding of coarse grains occurred at higher applied stresses than in the absence of fine-grained regions followed by an unaltered work-hardening rate at least up to approximately 1.5 % strain. In order to properly assess this finding, it must be noted that the separation of diffraction signal from fine and coarse grains in the absence of chemical or structural heterogeneity is challenging because of overlapping diffraction intensities. For achieving a separation between the two fractions, we developed a special algorithm based on differences in the integrated intensity between diffraction peaks from grains of different sizes [19].

In the present study, we monitored individual grains of different size in nickel samples with harmonic structure and individual coarse grains in a homogeneous coarse-grained structure during tensile deformation. To achieve that, we used high resolution reciprocal space mapping (HRRSM), which allows *in situ* monitoring diffraction peaks from individual grains embedded in the bulk during tensile loading [20,21]. The technique is selected because the diffraction peaks from individual grains can be traced in isolation from the background of very fine grains without using any separation algorithm and even small levels of plastic deformations can be detected at low strains. The transition from elastic to plastic deformation in an individual grain can be studied in detail through one of its diffraction peaks as its position in reciprocal space changes with elastic deformation and its appearance evolves with plastic deformation of the grain. The intensity distribution of such a diffraction peak represents local distortions of the crystalline lattice within an individual grain and is not completely smooth due to the formation of dislocation boundaries and subgrains [20,21]. Once yielding occurs, plastic deformation is carried by dislocations moving through the metal. A fraction of these dislocations becomes stored in the metal and self-organizes into dislocation structures. For face-centered cubic metals with medium to high stacking fault energies such as copper and nickel, dislocations typically form dislocation-rich walls separating dislocation-depleted regions called subgrains [21]. With HRRSM, the mean elastic strain of a grain and the local elastic strain of resolvable individual subgrains can be determined [20,21]. With increasing plastic deformation, more dislocations are generated, the subgrains decrease in size and the disorientations in the dislocation walls grow [22], which increases the lattice distortion [23]. The current study serves two purposes: (i) to investigate the behavior of individual coarse and fine grains in HS during tensile loading, and (ii) to gain further insights on how the behavior of coarse grains is affected by the enclosure by fine grains.

2. Experimental procedure

2.1. Material fabrication and characterization

Nickel powder with spherical particles of a mean diameter of 149 μm was produced through plasma rotating electrode processing (PREP). The chemical composition of the powder is summarized in Table 1. The spherical powder particles were mechanically milled with a planetary ball mill to produce a heterogeneity in grain size within each powder particle with coarse grains in the core and fine grains close to the particle surface constituting a shell. The powder was milled with high carbon steel balls (SUJ2, 9 mm in diameter) in a 500 ml vial made of tool steel (SKD11). The ball to powder weight ratio was 1.8:1. Balls, powder and 1 ml heptane used as processing control agent were added to the vial in an argon-filled glove box to assure processing in an oxygen free environment. The balls and the vial were reused from previous milling cycles of a nickel powder of similar quality. In this manner, balls and vessel had a nickel coating on the surface minimizing contamination. The processing control agent minimizes cold welding between balls and powder particles as well as between powder particles to avoid particle agglomeration. Mechanical milling was carried out at room temperature for 100 h with a rotation speed of 150 rpm. After processing, the powder was sieved through two meshes with opening sizes 212 μm and 100 μm to separate out agglomerated and fine fractured particles. Only the fraction of particles between 100 μm and 212 μm was retained.

To maintain the heterogeneous grain size after mechanical milling and to achieve fully dense compacts, spark plasma sintering (SPS) was applied. The milled powder was consolidated in vacuum atmosphere at 800 °C under a pressure of 100 MPa held for 30 min followed by furnace cooling from 800 °C to 525 °C in 2 min and slower subsequent cooling from 525 °C to 332 °C in 10 min to obtain HS compacts. Additionally, homogeneous coarse-grained compacts were fabricated from unprocessed initial powder using the same processing settings except for a higher sintering temperature of 850 °C. The final compacts were disks approximately 15 mm in diameter and 2.5 mm in thickness. Sections of the compacts were prepared for microstructural investigations by grinding on SiC paper followed by polishing with diamond suspension and finally with colloidal silica.

Microstructural observations were carried out using electron backscatter diffraction (EBSD) in a JEOL JSM 7100F operating at 15 kV with 15 mm working distance equipped with TSL OIM Data Collection software, while ion channeling contrast microscopy (ICCM) was conducted with an FEI Nova NanoLab 600 FIB/SEM.

For the synchrotron investigations, the dog-bone shaped tensile specimens with a nominal gauge length of 5 mm and a width of 1.5 mm were cut from the compacts by electric discharge machining. To enable sufficient X-ray transmission, their thickness was reduced by grinding and polishing to 0.8 mm and 0.7 mm for the HS and the reference coarse-grained samples, respectively.

The results of the microstructural observation are shown in Fig. 1 for the HS compact in Fig. 1a–d and for the compact produced from initial powder in Fig. 1e. A light-optical micrograph in Fig. 1a presents the periodic pattern of fine and coarse grains achieved in the HS compact at the macroscopic scale. Since grain sizes vary substantially within and between the compacts, different step sizes were used for acquiring the maps for EBSD analysis. For the boundary map of the HS compact (Fig. 1b), a step size of 0.5 μm was used. The large step size allowed acquiring a statistically significant representative number of larger grains, but the fine grains were not resolved. Therefore, grains at the periphery of powder particles (termed shell) appear black in the

Table 1
Chemical composition of pure nickel initial powder (wt %) from [24].

C	Si	Mn	S	Cu	Fe	Ni
0.03	0.05	0.15	0.01	0.01	0.39	99.36

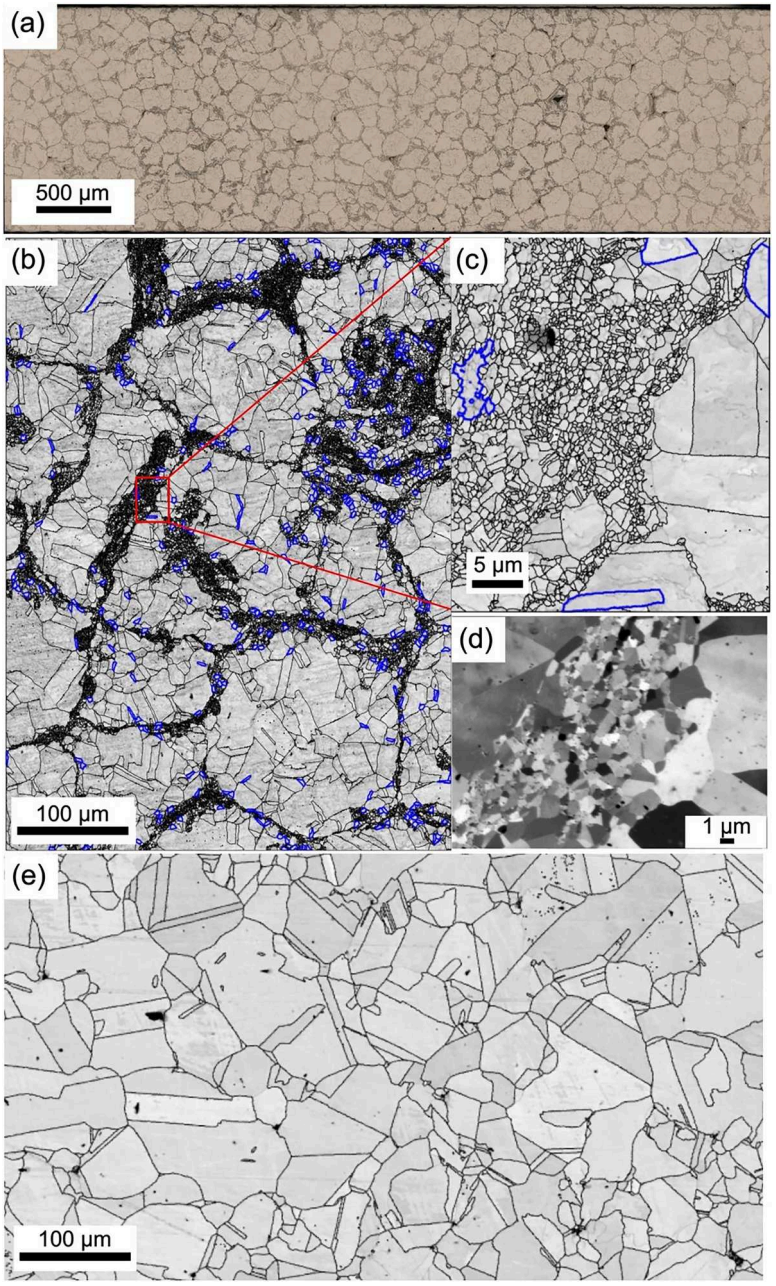

Fig. 1. The microstructure of harmonic-structure (a-d) and coarse-grained (e) nickel. The light-optical micrograph in (a) shows a rather regular, almost periodic pattern in the spatial distribution of grain sizes. EBSD image quality maps overlaid with high angle boundaries (≥15° misorientation) in (b) and (c) reveal further details of the structure of coarse grains in the core and fine grains in the shell areas, respectively. Grains with equivalent circular diameter between 4 µm and 5 µm are highlighted in blue in (b) and (c). Ion channeling contrast microscopy micrograph in (d) illustrates that some grains in the shell are ≤1 µm in size.

boundary map, while the grains in the core are clearly visible. Fig. 1a,b clearly display a core-shell structure characteristic for HS materials. The shell fraction was assessed by applying a threshold value for the grain size of 5 µm to distinguish between grains in the core and in the shell. Based on this method, 75 % of the grain area was determined to consist of grains larger than 5 µm and the remaining 25 % were assumed to be shell. To resolve details of the microstructure of the shell fraction, a map with a smaller step size of 0.1 µm was also acquired. As can be seen in the resulting boundary map (Fig. 1c), the shell comprises of fine grains. The map as well as the complementary ICCM micrograph (Fig. 1d) shows that some grains are ultrafine with a grain diameter smaller than 1 µm. When grains smaller than 5 µm are excluded, i.e. when only core regions are considered, the area-weighted mean grain size in the overview Fig. 1b is 21 µm. The shell in Fig. 1c predominately constitutes of grains in the range 0.5-3 µm. Figs. 1b,c highlight all grain with equivalent circular diameter between 4 µm and 5 µm revealing that grains with such sizes are mainly located within the network of forming the shell skeleton. For the compacts produced from the initial powder, an EBSD map was acquired with a step size of 0.6 µm. A corresponding image quality map overlaid with grain boundaries is shown in Fig. 1e revealing an area-weighted mean grain size of 49 µm.

2.2. *High resolution reciprocal space mapping*

High resolution reciprocal space mapping was carried out *in situ* during tensile testing at beamline P07 at PETRA III with a set-up similar to [25]. A sketch of the set-up is provided in Fig. 2. A monochromatic beam of 52.7 keV with low bandwidth was focused to 36 µm in vertical

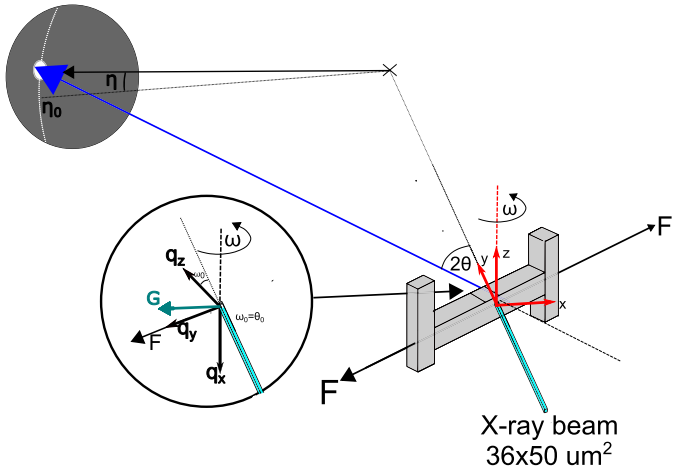

Fig. 2. Sketch of experimental set-up. The diffraction angle θ and the azimuthal angles η and ω are defined together with the real and reciprocal space coordinates.

direction and 107 μm in horizontal direction. The beam was further narrowed by slits in the horizontal direction to 50 μm so that the beam size became 36 μm by 50 μm in z- and x-direction, respectively. Diffraction spots were recorded on a MarCCD 165 area detector placed 3.9 m behind the sample at a horizontal position corresponding to the 400 diffraction peak of Ni from grains having their diffraction vector close to parallel to the tensile axis.

The specimens were mounted in a custom-made screw-driven load frame equipped with a 1 kN load cell in order to carry out interrupted *in situ* tensile tests and loaded with a small preload of 10 MPa for the HS specimen and a preload of 1 MPa for the reference specimen of homogeneous coarse grains. The load frame allowed for mechanical loading while investigating individual grains in the specimens by means of synchrotron radiation. The strain was measured by strain gauges glued on the center of the gauge section of the specimens aligned with the tensile axis, while the stress was determined with an integrated load cell. The load frame was placed horizontally on top of a set of translation and rotation stages that enabled the sample to be moved in x, y, and z, as well as rotations around the z-axis (i.e. rocking through the ω angle). The movement in x and z enabled the investigated grains to be re-centered in the beam when slightly displaced after each load step.

Prior to commencing the interrupted *in situ* tensile test, grains suitable for HRRSM needed to be identified based on the criteria specified in [23]. The grains have to be smaller than the beam to ensure that they are completely illuminated. The grains need to have their diffraction vector close to parallel to the tensile axis and no overlapping reflections from other grains must appear. Moreover, grains that have a too large orientation spread were excluded to minimize acquisition time when rocking around the z-axis. Suitable grains were found by rotating the load frame by an ω angle $\pm 10^{\circ}$ around the z-axis at different positions within the specimen by moving the specimen with the translation stages. When a suitable grain had been found, the grain was centered in the beam by scanning the sample in x- and z-direction. These centering scans also allowed the estimation of the grain size according to the procedure in appendix A.

Table 2 summarizes the details of grains selected for HRRSM. Two suitable grains (G1 and G2) were identified in the reference coarse-grained specimen. Similarly, two grains (LG1 and LG2) larger than 20 μm were selected in the harmonic structured specimen. Judging from their size, these grains must be located in the core of original powder particles despite being slightly smaller than the ones selected in the coarse-grained specimen. Furthermore, two more grains (SG1 and SG2) in the HS specimen were investigated. Their diffraction signals were identified in the detector images containing the diffraction peak of LG1.

Table 2
Overview of the selected grains in different specimens and their estimated grain size.

Specimen	Grain	Estimated grain size (μm)
Homogeneous coarse-grained	G1	37.3
	G2	39.1
Harmonic structured	LG1	21.0
	LG2	22.9
	SG1	3.9
	SG2	4.8

Compared to the LG1 and LG2, SG1 and SG2 are small with sizes below 5 μm implying that they are within or in close proximity to the fine-grained network (cf. Fig. 1b, c) but still too big to be representative of it. Consequently, for the HS specimens two different types of grains are investigated, two large (LG1 and LG2) from the coarse-grained cores and two small (SG1 and SG2) from the fine-grained network.

After identification of suitable grains and their mapping by HRRSM, *in situ* tensile testing was carried out. Each specimen was stepwise loaded in tension with stress increments of approximately 20 MPa. After each load step, each large grain (G1 and G2 in the reference and LG1 and LG2 in the HS) was centered in the beam by translating in x, z and rocking the angle ω to achieve maximum intensity of the diffracted signal prior to the acquisition of HRRSM data and to ensure that the grains are fully illuminated.

High resolution reciprocal space maps were acquired by rocking the sample around the z-axis with constant rotation speed over narrow intervals of $\Delta\omega = 0.01^{\circ}$. The intensity on the detector was recorded during an exposure time of 5 s. Adjacent ω intervals were stacked to gather reciprocal space maps in 3D. Each point in the 3D data set is assigned the rocking angle ω defined as the average ω-angle of its $\Delta\omega$ interval as well as two further angles defined by the pixel position on the detector: the diffraction angle θ (along the radial direction), and the angle η along the azimuthal direction [21].

Based on the diffraction angle θ, the length of the diffraction vector q is calculated by

$$q = |q| = \frac{4\pi}{\lambda} sin(\theta)$$

with a resolution of $\Delta q = 5.5 \times 10^{-4}$ Å^{-1} determined in [25].

By integrating the intensity along the diffraction vector for each (η,ω), an azimuthal map is obtained. The angles are converted to reciprocal space coordinates based on [26,27]

$$q_x = -(\eta - \eta_0)\frac{2\pi}{\lambda} sin(2\theta)$$

$$q_z = (\omega - \omega_0)\frac{4\pi}{\lambda} sin(\theta)$$

where η_0 and ω_0 are defined, when the diffraction vector of 400 diffraction peak is parallel to the tensile axis. The map reflects the orientation spread and mosaicity within the grain [23]. Furthermore, the average position of the intensity distribution from the grain in the azimuthal map reflects the angle between the tensile axis and the [100] direction [21]. Radial peak profiles are obtained by integrating the intensity perpendicular to the diffraction vector, i.e., along η_0 and ω_0, onto the diffraction vector. Such a projection results in a radial peak profile (showing the intensity in dependence of the diffraction angle θ) reflecting the distribution of distances between lattice planes within the grain and hence the elastic strains [25].

3. Results

3.1. Macroscopic mechanical behavior

True stress-strain curves of HS and coarse-grained Ni pulled at a strain rate of $3.6 \times 10^{-3}\ s^{-1}$ from [28] are shown in Fig. 3 overlain with the interrupted crosshead position-controlled measurements at the synchrotron facility during the acquisition of HRRSM data. The mechanical behavior of the studied specimens is consistent with the previous studies, as shown in Fig. 3. However, the strain gauge initially detected compressive strains for the HS specimen while pulling up to 92 MPa. This is regarded as a consequence of the specimen probably becoming slightly bent during mounting. Therefore, the strains were extrapolated for load step less than 92 MPa of the HS specimen based on the linear behavior between the loads of 125 MPa and 175 MPa to be able to compare the deformation behavior of the grains in both specimens at equivalent macroscopic strains. Table B.1 and B.2 in appendix B summarize the strains at the individual load steps shown in Fig. 3 for both specimens.

3.2. Evolution of individual grains

The 3D intensity distribution of the reflections is difficult to visualize, but the information of the distribution in orientation space can be presented in terms of azimuthal maps, and the distribution of elastic strains can be quantified through radial profiles. Fig. 4 displays the azimuthal maps of the reflection from LG1 with increasing applied load.

In order to enhance fine details, magnified contour maps of the reflection are shown in the series of insets at the lower part of each row. The contour map acquired at an applied load of 10 MPa shows that the intensity distribution is clearly heterogeneous with several peaks of high, but varying intensity. Each individual peak, i.e. each local maximum in reciprocal space, represents an individual dislocation-free subgrain [20,21,29]. The integrated intensity of such a peak scales with the size of the subgrain [20]. The change in total intensity between the full azimuthal maps is compensated for by scaling. The upper limits

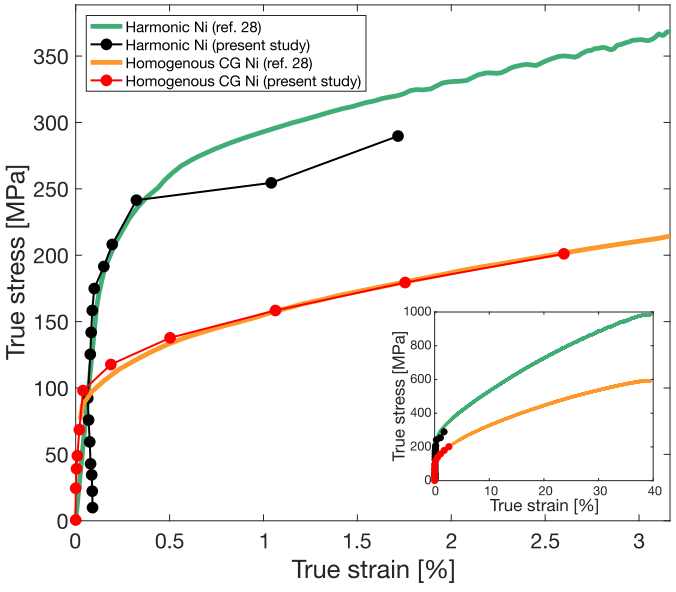

Fig. 3. True stress-strain curves during the elasto-plastic transition of HS Ni and the reference material of homogenous coarse grains. The inset displays stress-strain curves from the full tensile test. The curves with solid dots show the in situ experiment at the synchrotron facility, while the continuous curves show laboratory tests with the same settings of another specimen batch produced in the very same manner for comparison confirming the consistency of mechanical testing results.

of the color scales of the contour maps are set to reveal the structure of the peaks of lower intensity levels. The limits are kept as fixed as possible to facilitate comparison of the maps.

Comparison of the contour maps indicates that the overall azimuthal intensity distribution of the reflection is unchanged between stress levels from 10 to 92 MPa. During stress levels from 92 to 175 MPa small but clear changes are visible as those highlighted by black and red arrows. The highest intensity peak indicated by the black arrow splits into two peaks between 92 and 142 MPa which then move relative to each other when loading to 175 MPa. The peak indicated by red arrow displays similar behavior. The overall azimuthal intensity distribution changes considerably between 175 and 208 MPa and expands in the azimuthal directions as evident from the overview maps.

Inspection of the overview maps between 10 and 208 MPa shows that the intensity of the reflection outside the individual sharp peak increases. This part of the intensity distribution, also known as the cloud component, represents dislocation-rich walls that separate subgrains [21]. The increasing intensity of the cloud component indicates that the volume fraction of dislocation walls increases at the expense of the subgrain component. Using the algorithm described in references [23,30,31], it is possible to partition the azimuthal map into a subgrain and a cloud component for further quantification.

Azimuthal maps of SG1 constructed with the same method as for LG1 are shown in Fig. 5. The magnified contour maps indicate that the azimuthal intensity distribution does not change between 10 and 175 MPa. The reflection expands slightly in q_z at 191 MPa and clearly changes shape during subsequent stress increments. Interestingly, the peak splits into three at 252 MPa suggesting that subgrains do form even in relatively small grains.

The most suitable grains identified in the reference sample with homogenous coarse grains had a large orientation spread of 1.0° in ω (or 0.125 $Å^{-1}$) already prior to loading. In order to reduce the acquisition time, the full range in ω was captured with wide intervals $\Delta\omega = 0.2°$ and only a selected range in ω was mapped with narrow intervals $\Delta\omega = 0.01°$. Fig. 6 shows azimuthal maps of the part of G2 acquired with narrow $\Delta\omega$ intervals. The figure is constructed with the same method as for LG1.

Comparing the magnified contour maps from selected stress levels, the general structure of the intensity distribution is unchanged until a stress level of 69 MPa. The cluster of subgrains on the left side of the map subdivides into several subgrains at 118 MPa. The azimuthal intensity distribution changes completely at 157 MPa as shown in the overview maps.

Azimuthal maps constructed in the same manner are presented for grains LG2, SG2 and G1 in appendix C.

Radial profiles of the 400 reflection acquired at different load steps for the large grain LG2 of the HS specimen and for G2 in the reference specimen are shown in Fig. 7a and b, respectively. It reflects the distribution of lattice plane spacings between {100} planes perpendicular to a ⟨100⟩ direction. The profiles are fitted with a split pseudo-Voigt function and are characterized through average peak position q_{mean} and integral width β^g. The average peak position is defined as the average diffraction vector length weighted by intensity for all intensities above 1/50 of the maximum. The integral width is defined as the area under the radial profile for intensities above 1/50 of the maximum divided by the maximum intensity. The average peak position reflects the average elastic strain of the grain, while the integral width is a measure of the heterogeneous elastic strains and their distribution [26]. Dislocations within the subgrains, but predominately in the walls [26] are a source of the elastic strain distribution as well as differences in elastic strain among subgrains [26,27].

Fig. 8 shows the evolution of the characteristic, quantitative measures of the radial profiles in each investigated grain as well as that of the macroscopic strain with applied stress. Combination of changes in the azimuthal maps and integral width are indications whether a grain is deforming through elastic or plastic deformation. G1 and G2 in the

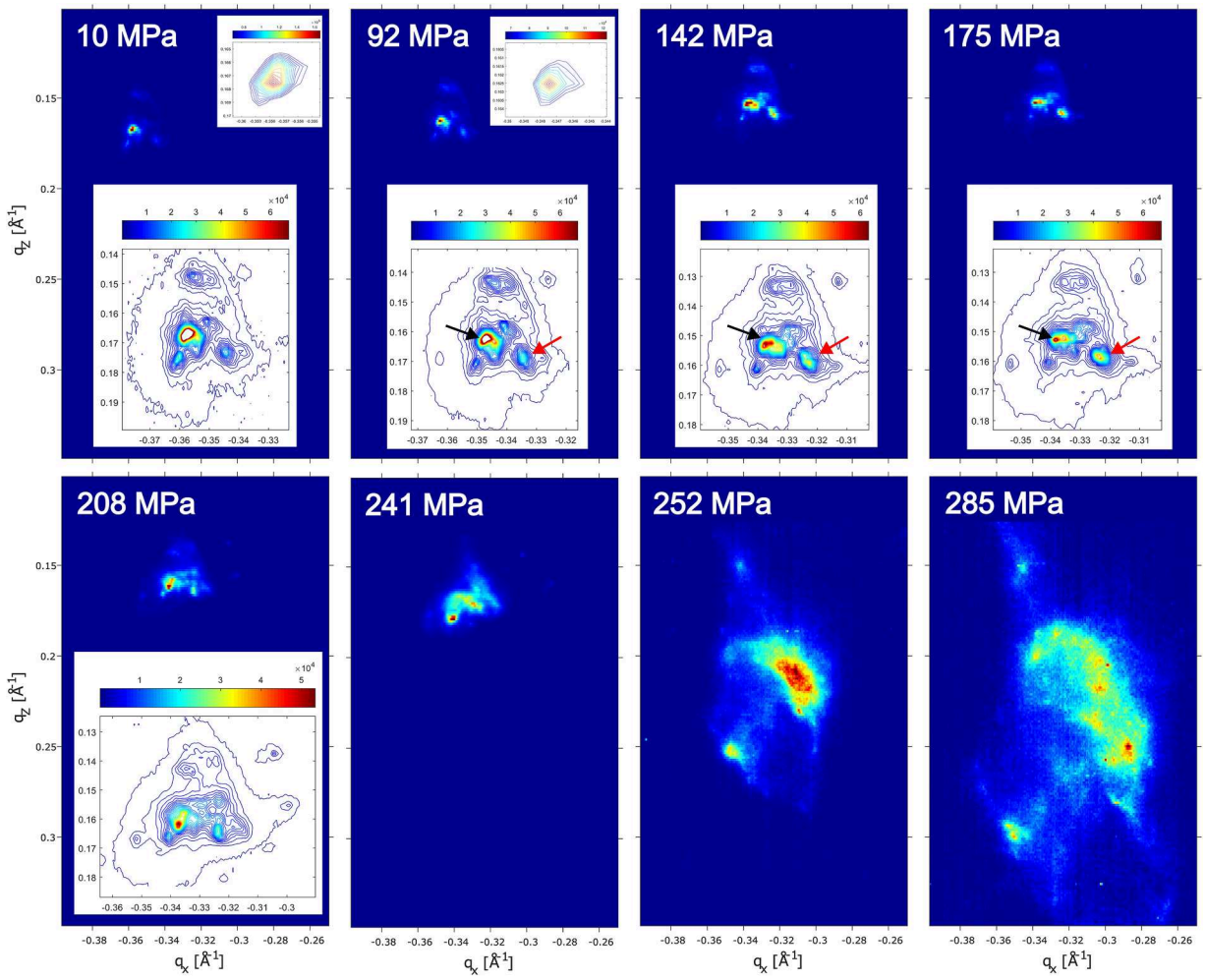

Fig. 4. Azimuthal maps of large grain LG1 in HS specimen. The colored maps represent the same region in reciprocal space to reveal changes in position and extent. They are scaled to 90 % of the maximum pixel intensity in the map. The contour maps in the insets reveal more details of the pole distribution and the presence of individual subgrains. The large insets at the lower part for the loads 10 MPa to 208 MPa are scaled to a fraction of the integrated intensity in the reflection. A fixed color scale is used for the applied loads of 10 to 175 MPa to facilitate identification of individual subgrains and monitoring their evolution. The smaller insets at the upper-right corners of the maps for applied loads 10 MPa and 92 MPa reveal the intensities above the threshold value.

reference specimen display the same behavior without any change in the azimuthal distribution and no increase of the integral width until 69 MPa, followed by clear changes in the azimuthal distribution and an increase of integral width. LG1 and LG2 in the HS specimen display similar behavior in the evolution of azimuthal intensity distribution with no obvious change between 10 MPa and 92 MPa, minor changes between 92 MPa and 175 MPa, and a clear change in appearance and expansion in the azimuthal directions thereafter. The integral width of LG1 remains almost constant until 175 MPa and increases clearly thereafter. LG2 has a similar behavior except that the integral width increases slightly during the sequence of stress increments until 175 MPa. For SG1, neither the intensity distribution of the reflection in the azimuthal map, nor the integral width change significantly until 175 MPa. The azimuthal intensity distribution changes slightly at 191 MPa, while the integral width clearly increases. Both measures clearly change from 191 MPa. Similar to SG1, SG2 neither changes its azimuthal intensity distribution, nor increases its integral width significantly until 92 MPa. However afterwards, its azimuthal distribution changes slightly until 142 MPa, and the integral width increases. The azimuthal distribution does not change significantly between 142 MPa and 175 MPa while the integral width continues to increase. In contrast to SG1, both the azimuthal distribution and the integral width of SG2 clearly change already from 175 MPa.

Summarizing the combination of qualitative (Figs. 4–7) and quantitative (Fig. 8) changes with increasing applied stress can be divided into three categories:

I. No change in azimuthal intensity distribution and no increase of integral width, which is interpreted as purely elastic deformation.
II. Minor change in azimuthal intensity distribution without clear increase of integral width. This is interpreted as small levels of plastic deformation.
III. Clear change in the appearance of azimuthal intensity distribution combined with an expansion in the azimuthal directions and a clear increase of the integral width. This is understood as significant plastic deformation.

The interpretations above are consistent with previous HRRSM studies on high purity copper showing that subgrains with an equivalent sphere diameter of 1.4 μm form after straining to 2 % [21]. Peak splitting into two subpeaks can be caused by a single dislocation in a subgrain [20,32]. Accordingly, the split of individual peaks from individual subgrains such as between the stress levels of 92 and 142 MPa for LG1 in Fig. 4 is considered to be associated with dislocation activity. Moreover, a similar sharp transition of the integral width as a function of applied stress as in Fig. 8a and b was observed for copper subjected to strain path

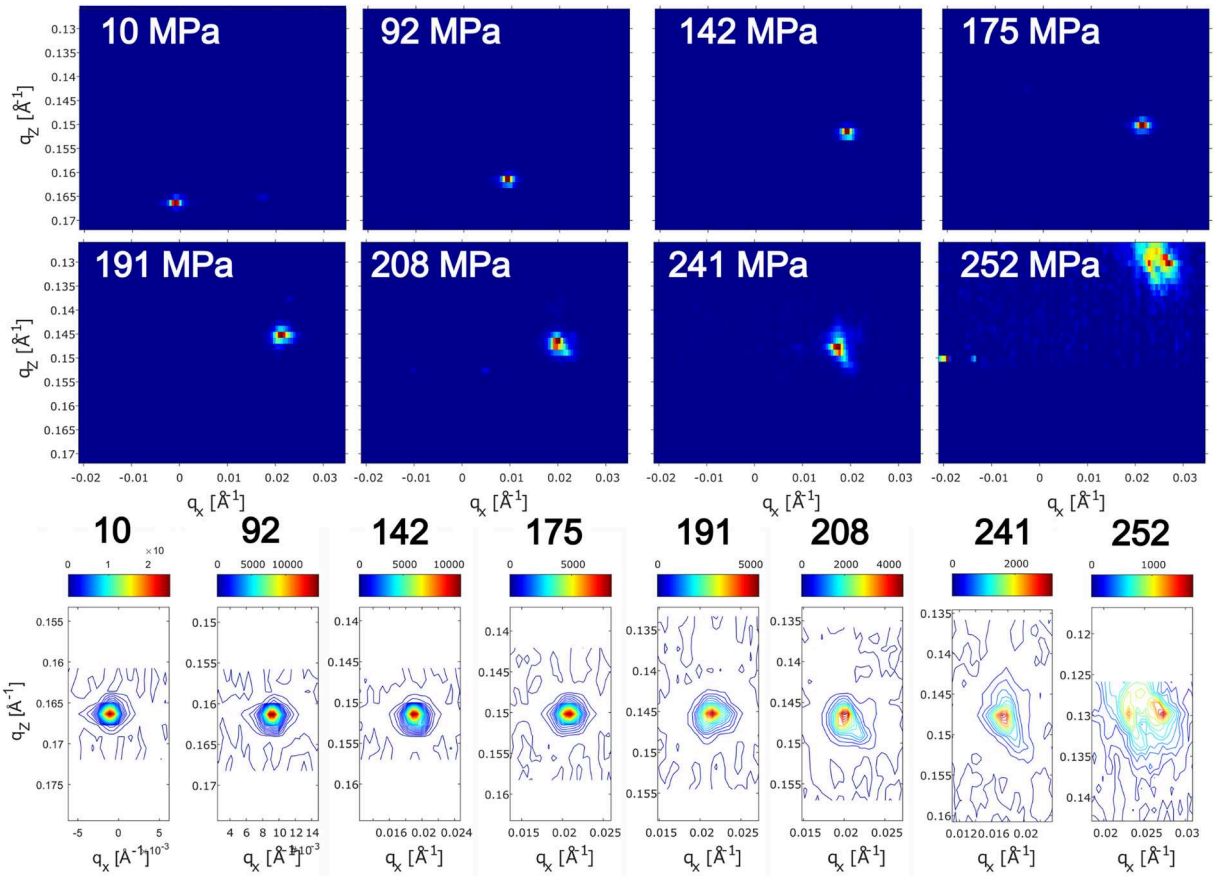

Fig. 5. Azimuthal maps of small grain SG1 in HS specimen. The upper series of maps represent a fixed region in reciprocal space to reveal changes in position and extent. They are scaled to 90 % of the maximum pixel intensity in the map. The bottom row of contour maps reveals more details of the pole distribution and the presence of individual subgrains. The contour maps are scaled to a fraction of the integrated intensity in the reflection.

changes [30]. The slowly increasing width at the small stresses was interpreted to originate from increasing variation of the intra-granular stresses among subgrains and the sharp increase from increasing dislocation density in the dislocation walls (due to dislocation accumulation).

Given the above arguments, it is concluded that all the investigated grains in the HS material deform by elastic deformation until 92 MPa. Thereafter, both large grains and the small grain SG2 display signs of small levels of plastic deformation while SG1 continues to deform elastically only. All the investigated grains show signs of significant plastic deformation from an applied stress of 175 MPa. The three different behaviors of the diffraction peaks are associated with three deformation regimes:

A Solely elastic deformation
B Onset of plastic deformation and
C Significant plastic deformation.

These regimes are identified in Fig. 8 by vertical black lines of constant stress levels. From regime C, a further regime D is distinguished, which will be explained later.

Grains in the sample with homogenous coarse grains deform through elastic deformation until 69 MPa and through significant plastic deformation onwards indicating the occurrence of regimes A and C only.

To further investigate the variation between the grains with respect to the onset of plastic deformation, the evolution of the mean radial peak position (given by the diffraction vector) with applied stress is discussed based on Fig. 8c and d. Relative differences in the diffraction vector q-q_0 are related to elastic strain:

$$\epsilon_{el} = \frac{d - d_0}{d_0} = \frac{q_0 - q}{q}$$

The strain-free diffraction vector $q_0 = 7.14$ Å^{-1} (based on the lattice constant of pure nickel $a = 3.52$ Å) is shown by dotted lines, and the average initial q_{ref} of several grains in the respective sample after mounting in dashed lines. q_{ref} was estimated by summing radial profiles from several grains acquired prior to loading. (Such radial profiles were obtained when locating grains in the specimen suitable for HRRSM. During the process of finding suitable grains, the specimen was rotated in ω and the beam was scanned in x and z over the specimen in large steps. By adding the radial profiles from all of these coarse scans and fitting the summarized peak with a split pseudo-Voigt function, the mean q of the peaks a q_{ref} of 7.1382 Å^{-1} and 7.1409 Å^{-1} was obtained for the HS and the homogenous coarse-grained sample, respectively).

The variation between the initial mean peak positions among the grains in the HS materials reveals significant internal stresses in the initial state. LG2 and SG2 show compressive strains compared to q_{ref} and LG1 and SG1 show tensile strains. The internal stresses may have developed either during the fabrication of the material or during specimen mounting. As a general trend, the mean positions of all grains shift to lower values with increasing applied stress due to the increasing lattice spacing along the [100] direction, which is close to the tensile axis. The slope of the solid black line corresponds to the expected decrease of the mean position with increasing applied stress based on the directional Young's modulus along the [100] direction (assuming unidirectional loading). Interestingly, none of the mean grain positions decrease linearly with applied stress. An apparent incremental elastic modulus $E^* = |\Delta\sigma|/|\Delta\epsilon_{el}|$ can be determined for each grain for the

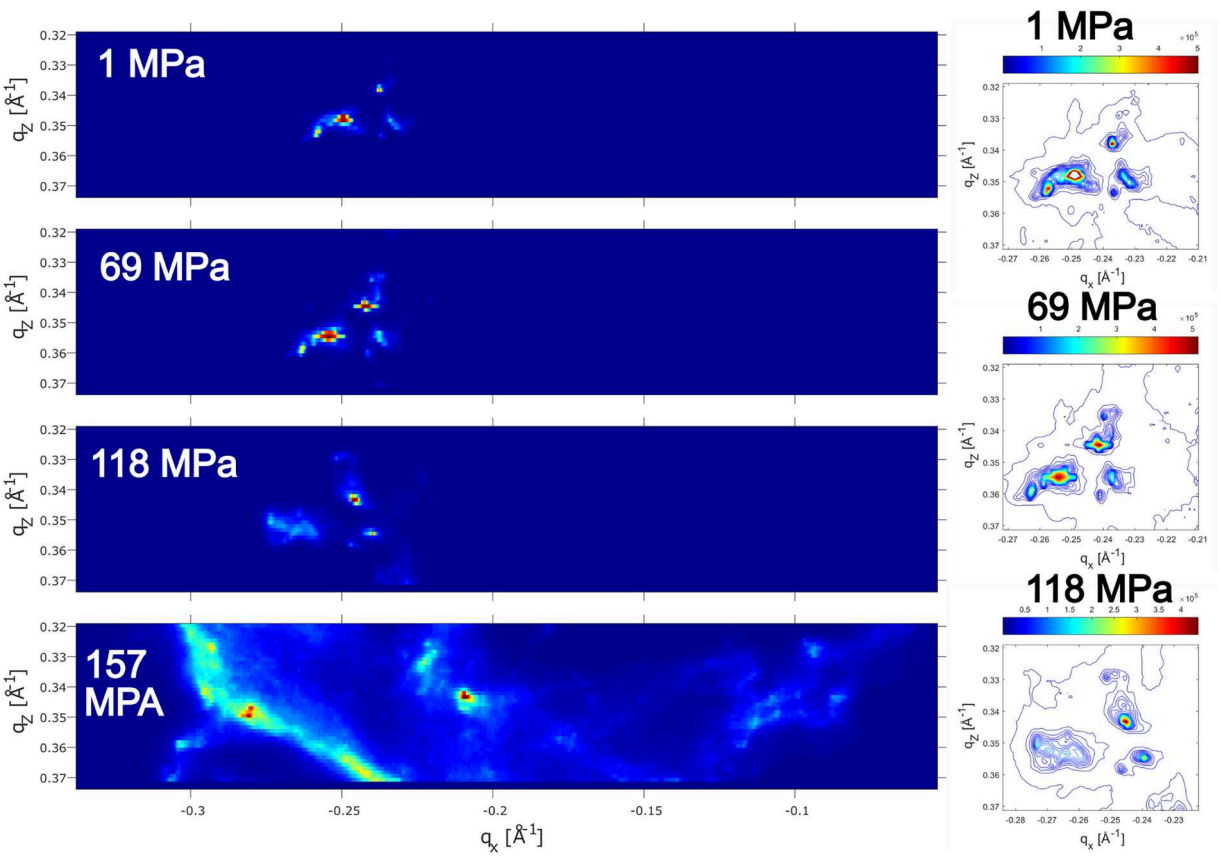

Fig. 6. Azimuthal maps of coarse grain G2 in coarse-grained reference specimen. The series of maps in the left column represents a fixed region in reciprocal space to reveal changes in position and extent. They are scaled to 90 % of the maximum pixel intensity in the map. The series of contour maps in the right column reveals more details of the pole distribution and the presence of individual subgrains. The contour maps are scaled to a fraction of the integrated intensity in the reflection.

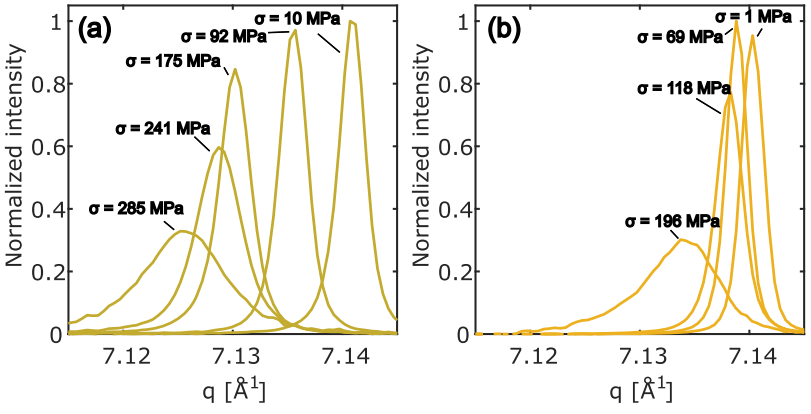

Fig. 7. Evolution of radial profiles with applied load for (a) LG2 and (b) G2.

different ranges $\Delta\sigma$ of applied stress. Such apparent incremental elastic moduli are estimated in different ranges and summarized in Table 3 and 4 for each grain based on clear transitions in the trends of decreasing diffraction vector lengths with increasing applied stress. During significant plastic deformation a clear change in the E^* of the large grains can be found, which motivates further subdivision into regimes C and D in the HS material.

4. Discussion

4.1. Variation of grain behavior in HS material

In regime A showing elastic deformation only, a clear correlation between the initial strain state and the apparent incremental elastic modulus (E^*) is observed. Grains with an initial compressive strain state have low E^*, while the grains with an initial tensile strain have high E^*. Fig. 8c shows that all four investigated grains in the HS specimen develop a similar absolute elastic strain at a stress level of 125 MPa, i.e. at the transition into regime B. The variation in E^* indicates that the applied load does not distribute homogenously through the sample

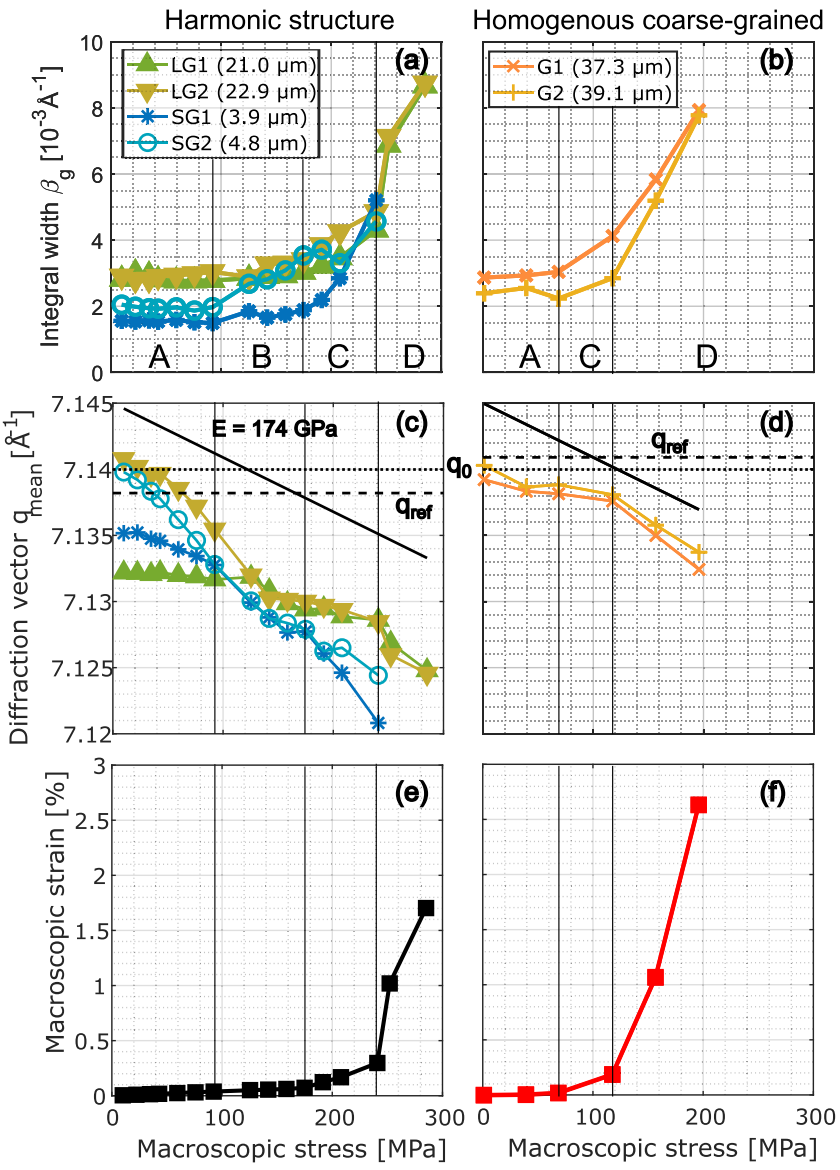

Fig. 8. Evolution of radial profiles in the selected grains (integral width, a-b, and peak position c-d) and extrapolated macroscopic strains for the HS (e) and the reference homogeneous coarse-grained (f) specimens with applied stress.

during regime A. The load rather seems to redistribute among the grains such that the stress homogenizes over the sample. At the border between regimes A and B, the stresses are similar among the grains.

Regime B shows signs of small levels of plastic deformation becoming visible for the large grains and the SG2. Notably, the grains have the most similar response to applied stress (in terms of E^*) between 125 and 142 MPa. When the plastic deformation becomes more pronounced between 142 and 175 MPa, E^* changes again. This is especially clear for LG2 which develops a particularly high E^* (see Table 3). The difference in E^* between LG1 and LG2 in the stress range indicates that the grains have very different neighborhoods (see appendix C) [33]. LG2 may have a plastically softer orientation than its close neighborhood and therefore yields before its surrounding. To deform compatibly with its neighborhood, LG2 develops back stresses compared to the applied load. This results in an extremely low slope in the stress range between 142 MPa and 175 MPa, i.e. a high E^* in Fig. 8c. Assuming that the Hall-Petch relation [3] holds for individual grains, small grains are in general inherently stronger than large grains and also have other small grains in their neighborhood due to the HS topology. Large grains can be either surrounded by other large grains (center of the core) or by small grains (core-shell interface). Forward stresses working opposite to back stresses develop in large grains and add to the applied stress in the small grains giving them higher elastic strain in regime B. Note, the small grains are not the smallest grains in the shell and may still develop back stresses in comparison with its smallest or stiffest neighbors. Note, SG2 shows small signs of plastic deformation, while SG1 does not. A higher resistance of SG1 against plastic yielding can be justified by its slightly smaller size.

Interestingly, SG2 shows signs of plastic deformation between 92 and 142 MPa, but the E^* is still low, Fig. 8. This may indicate that the SG2 changes shape slightly but is constrained by its neighbors such that continued deformation is possible through elastic deformation only. To summarize, regime B seems to be a transitional stage where the grains start to undergo varying levels of plastic deformation at different applied stresses depending on grain size and neighborhood.

The behaviors of the analyzed grains become more similar in regime C, as all grains show clear signs of significant plastic deformation. Nevertheless, there is a clear difference between the behavior of the large grains having high E^* and the small grains having low ones. This is reasonable given the different macroscopically averaged strain hardening rates of fine and coarse grains. Assuming that the strain is ho-

Table 3
Apparent incremental elastic moduli for grains in HS. Note that stress ranges with the same E^* appear because the presented value is the average E^* of that particular range. For highlighting the different values, the boxes are shaded according their relative values with green, yellow and red representing maximum, median, and minimum, respectively.

Regime	Stress (MPa)	LG1 E^* (GPa)	LG2 E^* (GPa)	SG1 E^* (GPa)	SG2 E^* (GPa)
A	10				
	22	217	178	--	115
	35	217	178	206	115
	43	217	178	206	115
	59	817	73	206	77
	76	817	73	206	77
	92	817	73	206	77
B	125	817	73	92	77
	142	137	73	92	77
	158	137	968	92	284
	175	137	968	--	284
C	191	443	301	68	133
	208	443	301	68	133
	241	443	301	68	133
D	252	84	75		
	285	84	75		

Table 4
Apparent incremental elastic moduli for grains in sample of homogenous coarse grains. For highlighting the different values, the boxes are shaded following the same color scale as in Table 3.

Regime	Stress (MPa)	G1 E^* (GPa)	G2 E^* (GPa)
A	1		
	39	409	231
	69	409	231
C	118	632	466
D	157	108	129
	196	108	129

mogenous over the core and the shell in a representative volume element in the sample up to 2 to 3 % strain [28,34], the small grains should attain higher stresses under the same level of plastic deformation. The small grains work harden faster than the large grains and therefore reach higher stresses, which results in lower E^*. The E^* are high for the LGs because back stresses continue to develop.

In regime D, the large grains have low E^*, and the intensity of the small grains becomes too smeared out in the azimuthal directions due to the plastic deformation to construct a characterizable radial profile. The lowering of E^* indicates that a larger part of the applied load concentrates in the large grains compared to the previous regimes of plastic deformation (B and C).

4.2. Difference in large-grain behaviors in HS and homogenous coarse grain materials

The investigated grains in the coarse-grained reference material show behavior different from the large grains of comparable size in the HS counterpart. The grains in the coarse-grained specimen deform through elastic deformation only up to 69 MPa, compared to 92 MPa in HS. Evident activity corresponding to regime B was not found but also cannot be excluded, as it might be hidden in the large stress increment from 69 MPa to 118 MPa. The most prominent difference between the materials is the onset of significant plastic deformation, which occurs already from 69 MPa in the coarse-grained material, compared to 175 MPa in HS. Comparing the mean peak position (or diffraction vector length) in Fig. 8, it is evident that the large grains in the HS specimen reach significantly higher stresses (manifested by smaller diffraction vector length) at the onset of regime C. This can be explained by the constriction of the large grains in the cores by the fine-grained network in the HS material. Under less constrained conditions in the CG material, the grains undergo plastic deformation at a lower applied stress.

Due to constriction by the network of hard fine grains, the large grains in HS material cannot deform freely and have to deform together with the surrounding matrix elastically. The elastic region therefore becomes extended to higher stresses as few, or no, surrounding grains deform plastically. In regime B, the large grains yield and deform plastically albeit to only a certain extent limited by still elastic deformation of most of the fine-grained network. This is particularly clear for LG1, which displays minor changes in the azimuthal map in 142 – 175 MPa range but a low E^* compared to LG2 in the same stress range and to both large grains in regime C. The low E^* suggests that LG1 deforms through elastic deformation or through plastic deformation with high strain-hardening in the range 142 – 175 MPa. Nevertheless, clearer changes in azimuthal maps and integral width similar to G2 (Fig. 6 and C.2) would be expected from high strain-hardening. When a large fraction of the fine-grained network deforms plastically, the constriction of the large grains decrease and they gain freedom for significant plastic deformation. At the same time, one must note that the smallest grains of the fine-grained network were not monitored individually meaning that at the onset of significant plastic deformation, grains of about 4 μm diameter and above certainly begin deforming plastically, while smaller grains in the network may still remain elastic.

The effects of neighboring grains are still visible in the coarse-grained material, although at a smaller stress range than in the HS one. G1 and G2 have high apparent incremental elastic moduli in regime C since back stresses develop due to their softer orientation compared to neighboring grains. In regime D, grains of most orientations (in the coarse-grained material), and also sizes (in the HS material), undergo plastic flow meaning that the individual grains are less affected by neighbors, which makes E^* in both the coarse-grained and the HS materials less different. More accurate comparison is difficult due to (i) still substantial differences in grain sizes and (ii) different evolution of local strains according to [28,34]

4.3. Comparison with average behavior of coarse-grained and fine-grained fractions in HS material

This study focusing on the behavior of individual grains agrees well with our previous study of the averaged behavior of the coarse and the fine-grained fractions in HS nickel [18]. Four stages of deformation were identified during the increase of applied stress:

- a stage of solely elastic deformation of fine and coarse grains until 130 MPa,
- followed by stress partitioning due to a mix of elastic and plastic deformation in the fine grains until 185 MPa simultaneous to plastic deformation in the coarse grains,
- then most fine grains also deform plastically, and stress partitioning continues due to a difference in strain-hardening rates between fine and coarse grains.
- Finally, at 240 MPa, the difference in local stresses between coarse and fine grains decreases [28,34] since strains and thus stresses start concentrating in the coarse grains.

In the current study, stress partitioning between large and small

grains occurs at a slightly lower applied stress of 125 MPa. At 191 MPa, all grains larger than 4 μm including SG2 are clearly in plastic deformation regime, while at least SG1 (smaller than 4 μm) might still be in the elastic deformation regime. From 175 MPa to 241 MPa, some differences in the amount of stress concentrated in the grains depending on size can be found. These are believed to be controlled by differences in strain hardening rates. After 241 MPa, stresses concentrate increasingly more in the large grains.

Comparison of the behavior of individual grains in this study with the separated behavior of the coarse-grained and the fine-grained fractions in the earlier investigation [18] reveals an impressive consistency. Such a consistency suggests that findings of this study on the example of just a few individual grains are sufficiently representative and can therefore be considered typical for the analysis of plastic deformation mechanisms in HS materials.

4.4. Relation to polycrystal modelling

The experimental findings obtained here shall briefly be discussed in the context of crystal plasticity based approaches used within solid mechanics for analytical modelling, e.g. [35]: HS must be considered as a dual-phase material with a single unit as representative volume element consisting of two phases (analogous to [36]), a coarse-grained core surrounded by a fine-grained shell. At the scale of such a unit, the elevated flow stress of HS at the elastic-plastic transition can be attributed to kinematic hardening at a single-grain level in both phases irrespective of scale. Namely, the formation of back stresses in the soft coarse grains leads to the translation of yield surface for each grain within the core, while the formation of forward stresses in the hard fine grains leads to a translation of yield surface of the grains in the shell. Although the directions of these translations are of opposite sign for the two phases and may vary from grain to grain within each phase, their net effect will be kinematic hardening as observed during regime B in the HS material.

It should be noted that recent results of crystal plasticity modelling on grain structures with grain size gradients or bimodal grains size distributions rationalize their mechanical behavior even without involving kinematic hardening [37,38]. In gradient-structured copper, isotropic hardening from forest dislocations has a stronger effect than the kinematic hardening [37], which agrees well with our observations at the developing regime D. Simulations of AISI 316 L steel with bimodal grain size distribution also showed an increase in the yield strength of the coarse-grained fraction compared to the homogenous counterpart [38].

An interesting similarity arises between the experimental results presented here and the thick yield surface concept [39]. Utilizing a cellular-automata based micro-mechanical model, it was proposed to model a polycrystalline material by a combination of multiple yield surfaces, i.e. a so-called thick yield surface, leading to a diffuse yield in varying combinations of principal stresses in the each grain of a polycrystal. The evolution of the stress cloud obtained in [39] closely resembles the evolution of internal stresses in our present study which advocates for the validity of arguments in both the works.

These comparisons suggest that the grain-level mechanisms of deformation in each phase of HS materials are neither unique, nor fully consistent with earlier experimental and theoretical findings. Concomitantly, the unique mechanical properties of HS material are a synergetic consequence of co-deformation of the fine- and coarse-grained phase at meso–scale within the unique architecture.

5. Conclusions

Reciprocal space maps of 400 reflections from four bulk grains in harmonic structure nickel and two in a coarse-grained sample with homogenous grain size were obtained in several steps until 1.7 and 2.6 % tensile strain, respectively. The two large grains with sizes of approximately 20 μm belong to the coarse grains in the core of the harmonic structure, and the small grains of sizes 3.9 and 4.8 μm represent the bigger grains in the fine-grained network. The two grains in the coarse-grained sample had a size of 40 μm. Reciprocal space maps allow tracking the mode of deformation in individual grain. The main results regarding the mode of deformation are:

- A transitional macroscopic regime of deformation is identified in the HS material where the individual grains switch from elastic to plastic deformation and undergo varying levels of plastic deformation at different applied stresses depending on grain size and neighborhood. The initial small levels of plastic deformation of the large grains transition to significant plastic deformation once a large fraction of the fine-grained network deforms plastically.
- After the onset of significant plastic deformation, the initial work-hardening rates increase with decreasing grain size for the small grains.
- Compatible deformation of the grains is ensured by the development of back stresses in the large grains and forward stresses in the small grains.
- The onset of significant plastic deformation of large grains in the HS material occurs at approximately 100 MPa higher stress than in the coarse-grained sample grains. This gap cannot be solely attributed to the difference in grain size and is attributed to the fact that fine grains constrain the large grains from deforming plastically in the HS material.

The latter finding exemplifies the potential of increasing the flow stress of coarse (large) grains in materials with micro-architected heterogeneous structures. Further studies are necessary to clarify the effect at later stages of plastic deformation of HS materials as well as those with other architecture designs.

Declaration of interests

The authors declare that they have no known competing financial interests or personal relationships that could have appeared to influence the work reported in this paper.

Acknowledgment

We acknowledge the support of DESY (Hamburg, Germany), a member of the Helmholtz Association HGF, for the provision of the synchrotron facility. The authors gratefully acknowledge financial support from Swedish Research Council (Vetenskapsrådet) research grant 2016-03811, the Swedish Foundation for International Cooperation in Research and Higher Education (STINT) grants SJ2017-7432 and MG2019-8450, and Interreg program “ESS & MAX IV: Cross Border Science and Society”, grants DTU007 and LU070. The experiment was carried out at beamline P07 with the aid of staff from P21.2 (beamtime experiment I-20170726 EC). The research leading to this result has also been supported by the project CALIPSOplus under the Grant Agreement 730872 from the EU Framework Programme for Research and Innovation HORIZON 2020. Nobuhiro Tsuji, Kei Ameyama and Dmytro Orlov were financially supported by the JSPS bilateral international collaboration with Sweden (grant JPJSBP120209918).

Supplementary materials

Supplementary material associated with this article can be found, in the online version, at doi:10.1016/j.actamat.2023.119623.

References

[1] M.A. Meyers, A. Mishra, D.J. Benson, Mechanical properties of nanocrystalline materials, Prog. Mater. Sci. 51 (2006) 427–556.

[2] K.S. Kumar, H. Van Swygenhoven, S. Suresh, Mechanical behavior of nanocrystalline metals and alloys11 the golden jubilee issue selected topics in materials science and engineering: past, present and future, edited by, in: S. Suresh (Ed.), Mechanical behavior of nanocrystalline metals and alloys11 the golden jubilee issue selected topics in materials science and engineering: past, present and future, edited by, Acta Mater. 51 (2003) 5743–5774.
[3] Y. Estrin, A. Vinogradov, Extreme grain refinement by severe plastic deformation: a wealth of challenging science, Acta Mater. 61 (2013) 782–817.
[4] Y. Zhu, K. Ameyama, P.M. Anderson, I.J. Beyerlein, H. Gao, H.S. Kim, E. Lavernia, S. Mathaudhu, H. Mughrabi, R.O. Ritchie, N. Tsuji, X. Zhang, X. Wu, Heterostructured materials: superior properties from hetero-zone interaction, Mater. Res. Lett. 9 (2021) 1–31.
[5] G. Li, M. Liu, S. Lyu, M. Nakatani, R. Zheng, C. Ma, Q. Li, K. Ameyama, Simultaneously enhanced strength and strain hardening capacity in FeMnCoCr high-entropy alloy via harmonic structure design, Scr. Mater. 191 (2021) 196–201.
[6] B. Sharma, G. Dirras, K. Ameyama, Harmonic Structure design: a strategy for outstanding mechanical properties in structural materials, metals (2020).
[7] Y. Xia, K. Miao, H. Wu, L. Geng, C. Xu, C.S. Ku, G. Fan, Superior strength-ductility synergy of layered aluminum under uniaxial tensile loading: the roles of local stress state and local strain state, Int. J. Plast. 152 (2022) 103240.
[8] F. Liang, B. Zhang, Y. Yong, X.M. Luo, G.P. Zhang, Enhanced strain delocalization through formation of dispersive micro shear bands in laminated Ni, Int. J. Plast. 132 (2020) 102745.
[9] S.K. Vajpai, M. Ota, Z. Zhang, K. Ameyama, Three-dimensionally gradient harmonic structure design: an integrated approach for high performance structural materials, Mater. Res. Lett. 4 (2016) 191–197.
[10] D. Orlov, K. Ameyama, Critical Assesment 37: harmonic-structure materials idea, status and perspectives, Mater. Sci. Technol. 36 (2020) 517–526.
[11] K. Ameyama, F. Cazes, H. Couque, G. Dirras, S. Kikuchi, J. Li, F. Mompiou, K. Mondal, D. Orlov, B. Sharma, D. Tingaud, S.K. Vajpai, Harmonic structure, a promising microstructure design, Mater. Res. Lett. 10 (2022) 440–471.
[12] A. Considère, Memoire sur l'emploi du fer et de l'acier dans les constructions, Annales des Ponts et Chaussées I sem (1885) 574–775.
[13] I.S. Yasnikov, A. Vinogradov, Y. Estrin, Revisiting the Considère criterion from the viewpoint of dislocation theory fundamentals, Scr. Mater. 76 (2014) 37–40.
[14] M.F. Ashby, The deformation of plastically non-homogeneous materials, the philosophical magazine: a, Philos. Mag. (1798-1977) 21 (1970) 399–424.
[15] H.K. Park, K. Ameyama, J. Yoo, H. Hwang, H.S. Kim, Additional hardening in harmonic structured materials by strain partitioning and back stress, Mater. Res. Lett. 6 (2018) 261–267.
[16] D. Orlov, R. Kulagin, Y. Beygelzimer, Strain partitioning and back-stress evaluation in harmonic-structure materials, Mater. Lett. 275 (2020) 128126.
[17] A. Shokry, A. Ahadi, P. Ståhle, D. Orlov, Improvement of structural efficiency in metals by the control of topological arrangements in ultrafine and coarse grains, Sci. Rep. 11 (2021) 17445.
[18] E. Sjögren-Levin, W. Pantleon, A. Ahadi, Z. Hegedüs, U. Lienert, N. Tsuji, K. Ameyama, D. Orlov, Stress partitioning in harmonic structure materials at the early stages of tensile loading studied *in situ* by synchrotron X-ray diffraction, Scr. Mater. 226 (2023) 115186.
[19] E. Sjögren-Levin, W. Pantleon, A. Ahadi, Z. Hegedüs, U. Lienert, N. Tsuji, K. Ameyama, D. Orlov, Separation of XRD peak profiles in single-phase metals with bimodal grain structure to analyze stress partitioning, IOP Conf. Ser. Mater. Sci. Eng. 1249 (2022) 012040.
[20] B. Jakobsen, H.F. Poulsen, U. Lienert, J. Almer, S.D. Shastri, H.O. Sørensen, C. Gundlach, W. Pantleon, Formation and subdivision of deformation structures during plastic deformation, Science 312 (2006) 889.
[21] B. Jakobsen, H.F. Poulsen, U. Lienert, W. Pantleon, Direct determination of elastic strains and dislocation densities in individual subgrains in deformation structures, Acta Mater. 55 (2007) 3421–3430.
[22] W. Pantleon, Disorientations in dislocation structures, Mater. Sci. Eng.: A 400-401 (2005) 118–124.
[23] W. Pantleon, C. Wejdemann, B. Jakobsen, U. Lienert, H.F. Poulsen, Evolution of deformation structures under varying loading conditions followed in situ by high angular resolution 3DXRD, Mater. Sci. Eng. A Struct. Mater. 524 (2009) 55–63.
[24] M. Nagata, N. Horikawa, M. Kawabata, K. Ameyama, Effects of microstructure on mechanical properties of harmonic structure designed pure Ni, Mater. Trans. 60 (2019) 1914–1920.
[25] A.M. Diederichs, F. Thiel, T. Fischer, U. Lienert, W. Pantleon, Monitoring microstructural evolution *in-situ* during cyclic deformation by high resolution reciprocal space mapping, J. Phys. Conf. Ser. 843 (2017) 012031.
[26] W. Pantleon, C. Wejdemann, B. Jakobsen, U. Lienert, H.F. Poulsen, Advances in characterization of deformation structures by high resolution reciprocal space mapping, in: N. Hansen, D. Juul Jensen, S.F. Nielsen, H.F. Poulsen, B. Ralph (Eds.), Proceedings Risø International Symposium on Materials Science, 2010, pp. 79–100.
[27] C. Wejdemann, H.F. Poulsen, U. Lienert, W. Pantleon, *In situ* observation of the dislocation structure evolution during a strain path change in copper, JOM 65 (2013) 35–43.
[28] D. Orlov, J. Zhou, S. Hall, M. Ota-Kawabata, K. Ameyama, Advantages of architectured harmonic structure in structural performance, IOP Conf. Ser. Mater. Sci. Eng. 580 (2019) 012019.
[29] B. Jakobsen, U. Lienert, J. Almer, H.F. Poulsen, W. Pantleon, Direct observation of strain in bulk subgrains and dislocation walls by high angular resolution three-dimensional X-ray diffraction, Mater. Sci. Eng. A 483-484 (2008) 641–643.
[30] C. Wejdemann, Evolution of dislocation structures following a change in loading conditions studied by in situ high resolution reciprocal space mapping. Technical University of Denmark, Risø National Laboratory for Sustainable Energy, 2011.
[31] C. Wejdemann, U. Lienert, H.B. Nielsen, W. Pantleon, Identifying individual subgrains in evolving deformation structures by high angular resolution X-ray diffraction, in: N. Hansen, D. Juul Jensen, S.F. Nielsen, H.F. Poulsen, B. Ralph (Eds.), Proceedings Risø International Symposium on Materials Science, 2010, pp. 477–487.
[32] B. Jakobsen, In-situ studies of bulk deformation structures: static properties under load and dynamics during deformation, Roskilde University, Roskilde, 2006.
[33] A.M. Diederichs, U. Lienert, W. Pantleon, Monitoring microstructural evolution in-situ during cyclic loading with high-resolution reciprocal space mapping, IOP Conf. Ser. Mater. Sci. Eng. 580 (2019) 012004.
[34] J. Chatellier, E. Sjögren-Levin, K. Ameyama, D. Orlov, Mechanics of accelerated strain hardening in harmonic-structure materials, IOP Conf. Ser. Mater. Sci. Eng. 1249 (2022) 012012.
[35] U.F. Kocks, C.N. Tomé, H.R. Wenk, Texture and Anisotropy: Preferred Orientations in Polycrystals and Their Effect on Materials Properties, Cambridge University Press, 2000, pp. 326–389.
[36] H. Liu, W. Pantleon, L. Mishnaevsky, Non-equilibrium grain boundaries in titanium nanostructured by severe plastic deformation: computational study of sources of material strengthening, Compute. Mater. Sci. 83 (2014) 318–330.
[37] X. Zhang, J. Zhao, G. Kang, M. Zaiser, Geometrically necessary dislocations and related kinematic hardening in gradient grained materials: a nonlocal crystal plasticity study, Int. J. Plast. 163 (2023) 103553.
[38] C. Keller, M. Calvat, B. Flipon, F. Barbe, Experimental and numerical investigations of plastic strain mechanisms of AISI 316L alloys with bimodal grain size distribution, Int. J. Plast. 153 (2022) 103246.
[39] Y.E. Beygelzimer, A.V. Spuskanyuk, The thick yield surface: idea and approach for investigating its structure, Philos. Mag. A 79 (1999) 2437–2459.